DSN 34-Meter Antenna Optics Analysis for Wideband SETI Investigations

S. D. Slobin
Radio Frequency and Microwave Subsystems Section

A DSN 34-meter symmetric Cassegrain antenna configuration is examined for wideband use over the frequency range of 1 to 10 GHz, rather than only at the narrow-band operational design frequencies of 2.295 GHz (S-band) and 8.448 GHz (X-band). Aperture efficiency and surface efficiency are calculated as the components determining the gain of the antenna. Noise temperature contributions arise from the ground, atmosphere, and quadripod scattering. These components are calculated as a function of frequency and elevation angle to determine a G/T (gain/system noise temperature) figure-of-merit for a nominal 34-meter antenna configuration. A computational method has been developed which will enable design of a multi-horn antenna feed system to optimally cover the 1 to 10 GHz frequency range.

I. Introduction

The SETI Project (Search for Extra-Terrestrial Intelligence, Refs. 1 and 2) is planning to investigate a small region of the microwave spectrum in its search for signals possibly indicative of life elsewhere in our galaxy. In particular, it has been decided that the region 1 to 10 GHz may be a particularly fruitful frequency band, based on considerations of galactic noise interference below 1 GHz, atmospheric noise above 10 GHz, and "philosophical" arguments regarding the "water-hole" communication frequency region from 1.4 to 1.7 GHz.

Clearly, the use of the Deep Space Network antennas would be of great value to SETI, as the cumulative collecting area of the 10 large antennas (ranging in size from 26-meter diameter to 70-meter diameter as of 1987) will be greater than that of any other assembly in the world, except those of the VLA (Very Large Array) in New Mexico. The three DSN antennas in Australia give access to the southern skies for declinations less than about -45°, a region unreachable by most of the world's large antennas. (An arbitrary southern elevation angle limit of 10 degrees is chosen to limit atmospheric effects and horizon mask noise contributions.)

The particular SETI search strategy contemplated is to use the 64-/70-meter antennas to look at particular stars (approximately 1000) in the frequency range 1 to 3 GHz. The 34-meter (or 26-meter) antennas will be used for an all-sky survey over the frequency range 1 to 10 GHz.

The DSN antennas, however, have been designed and built to operate at the specific narrow-band microwave frequencies used to communicate with "deep space" spacecraft, almost exclusively those launched by the United States. ("Deep space" is used to denote a distance from the earth generally beyond the orbit of the moon, 400,000 km.) Those

particular narrow-band (0.2 GHz) frequencies are L-band (1.7 GHz), S-band (2.3 GHz), and X-band (8.4 GHz); and L-band is presently carried only upon the 64-meter subnet.

II. Antenna and Feed Description

A typical 34-meter antenna is the DSS-12 instrument at Goldstone (Fig. 1). This antenna is a HA-DEC antenna; i.e., it is constructed to track in hour angle and declination, rather than in azimuth and elevation (AZ-EL). The 64-meter antennas (DSS-14, -43, -63) and new high-efficiency shaped-reflector 34-meter antennas (e.g. DSS-15) are of the AZ-EL configuration. A general description of all DSN antennas and microwave systems is given in Ref. 3. DSS-12 has a reflex feed type of microwave optics system whereby simultaneous S-band and X-band signals can be transmitted and received by use of the ellipsoidal reflector at the S-band feedhorn and a dichroic plate located over the X-band feedhorn. A complete description of this system is given in Ref. 4.

Because the dichroic plate is an inherently narrow-band device (8.3–8.5 GHz), use of the reflex feed system is contraindicated for SETI X-band investigations. The present analysis of the 34-meter microwave optics system then assumed that modification to the antenna would be necessary for wide-band use – certainly the reflex feed system would be eliminated. Possibly, a complete new series of feedcones and horns might be developed to cover the 1 to 10 GHz band.

In the reflex feed system, the subreflector is both tilted and of asymmetric shape. This design does not easily lend itself to use in configurations other than that for which it is specifically designed. The use of off-axis feedhorns in the asymmetric system would result in greatly reduced antenna gain and increased spillover and ground noise contribution.

A symmetric antenna with a single frequency corrugated feedhorn does not exist in the DSN. Modifications to existing antennas could create one; and for SETI use it may become necessary to operate in some slightly modified version of this simple antenna optics scheme. The basis of the analysis presented here was the 34-meter symmetric antenna design because it is very representative of performance obtained in both the asymmetric 34-meter and 64-meter reflex-feed antennas, and symmetric 26-meter antenna with an S-X common aperture feedhorn. Naturally, the gain differences between these different size antennas must be accounted for in the analysis.

An "equivalent" symmetric Cassegrain antenna was chosen for analysis. This antenna closely matches the DSS-12 34-meter design. Figure 2 and Table 1 show the actual antenna dimensions used in the analysis. Figure 3 and Table 2 show the dimensions of the subreflector, including the two-segment vertex plate used to direct reflected energy away from the feedcone area, and the peripheral flange used to control rear spillover and ground noise contribution.

The X-band feedhorn used in this analysis is identical to the X-band corrugated horn actually used in the reflex feed design. The S-band horn analyzed here is scaled (in size) by frequency (8.448/2.295) from the X-band dimensions. It is assumed in this analysis that the horns can be mounted separately with their phase centers (at the nominal design frequencies of 2.3 and 8.4 GHz) at the identical location relative to the antenna reflecting surfaces.

Most figures and tables in this report have dimensions given in inches. Although use of the English system of units is not a TDA reporting policy, these dimensions are already on design documents and blueprints, and comparison with existing documents is facilitated. Use of the metric system in this instance is not recommended.

III. Description of Computational Techniques

A description of the computational methods used to characterize antenna performance can be more easily understood by reference to Figs. 2 and 3. The goal of the analysis is to determine a G/T (gain/system noise temperature) for the antenna system at various frequencies and elevation angles. Table 3 shows the pertinent components of G and T.

It was decided to reference the computed G/T figures-of-merit to the G/T at the nominal S- and X-band frequencies (rounded off to 2.3 and 8.4 GHz) and elevation angle (90°), since the actual gains and system noise temperatures are published (Ref. 5) and presumably well known for these conditions. For a DSN 34-meter antenna of the DSS-12 type, the gain and zenith system noise temperature are 56.1 dBi and 21.5 K at S-band, and 66.2 dBi and 25.0 K at X-band. Actual system noise temperatures may be lower than these published numbers, especially in the case of a non-reflex antenna configuration. The G/T figure-of-merit can be expressed as (cf. Table 3)

$$G/T \sim \frac{\eta_{\text{aperture}} \times \eta_{\text{surface}}}{T_{\text{ground}} + T_{\text{atmosphere}} + T_{\text{quadripod}} + T_{\text{base}}} \quad (1)$$

Aperture efficiency is calculated as a percentage of the gain achieved by a (theoretically optimum) uniformly illuminated aperture, equal in size to the physical area of the antenna; or,

in other words, the gain of a uniformly illuminated aperture reduced by corrections for forward and rear spillover, non-uniform amplitude illumination, non-uniform phase illumination, cross polarization, and subreflector blockage. Quadripod blockage is not considered, as it is considered constant with frequency and elevation angle and is only a multiplicative constant in the numerator of Eq. (1) (an additive constant in terms of decibels). Quadripod blockage is already included in the published gain values for the DSN antennas.

Surface efficiency shows the effect of antenna main reflector surface roughness and deviation from a true paraboloidal shape as a result of gravity deformation. Ground noise arises from the "hot" earth's surface being reflected principally from the hyperboloidal subreflector into the feedhorn. Atmospheric noise (clear air) arises from oxygen and water vapor emission being reflected from the subreflector into the feedhorn (as in the case of ground noise) or from the atmosphere in the main antenna beam. Quadripod scatter noise results from the ground emission reflecting from the quadripod truss structure, and through one or more reflections entering the feedhorn.

The baseline system noise temperature is a constant for each microwave band and represents the "non-changing" contributions from the maser, waveguide (including horn), and cosmic background noise temperatures. The baseline values used here are 14.81 K (S-Band) and 18.25 K (X-Band).

All these components of G/T will be described further in more detail. The computational method proceeds as follows.

A. Corrugated Horn Patterns

Horn patterns are calculated from JPL Telecommunications Division computer programs known generically as "hybrid mode" programs. Geometrical inputs to these programs are given in Table 4. First, the illumination pattern of the existing X-band horn is calculated at 8.4 GHz using the physical dimensions of the horn. A subroutine in the program calculates a best-fit phase center of the horn pattern over a far-field polar angular extent of 16 degrees, the angle subtended by the subreflector (32 degrees from side-to-side). In the 8.4 GHz case, the far-field phase center is found to be located 2.2129 inches inside the horn aperture; and on the real DSS-12 antenna (and on our hypothetical antenna) the horn is physically located so that the phase center is coincident with the focus of the hyperboloidal subreflector (cf. Fig. 2). Calculations are made at other frequencies in the X-band range, and the calculated phase centers change from that at 8.4 GHz. These positions vary from 1.2 inches at 7.0 GHz to 3.4 inches at 9.4 GHz. The S-band positions vary from 3.6 inches to 15.7 inches over the frequency range 1.8 to 2.7 GHz. The analysis presented here assumes that the feedhorns cannot be repositioned to accommodate the changing phase center positions. Adjusting the subreflector position will not properly solve this misfocusing problem. The only proper solution is to accurately position the feedhorn as a function of frequency.

The S- and X-band frequency ranges are chosen to reflect the inherent bandwidth limitations of these particular DSN corrugated horns. The actual S-band range (modeled from X-band) would be 1.9 to 2.6 GHz, slightly narrower than that investigated here.

The changing phase center positions (which are not compensated for by repositioning the horn from its bolted-in 8.4 GHz or 2.3 GHz location) result in over- and under-illumination of the subreflector in addition to phase errors of up to a wavelength.

Figure 4 shows a typical X-band horn pattern at 8.4 GHz. Patterns at other frequencies (both X-band and S-band) are quite similar and are characterized by nearly identical E- and H-plane gain, and very low side and backlobes. Table 5 shows the 3-dB beamwidth, hyperboloid edge illumination, and phase center position for all S-band and X-band cases. Note that as the frequency increases from the nominal design frequency, the beamwidth decreases and the hyperboloid edge illumination decreases, resulting in under-illumination of the main reflector and decreased aperture efficiency. At frequencies lower than the design frequency, beamwidth and illumination increase, and rear spillover increases, thus increasing contribution from ground emission. For all cases, the horn patterns are stored in computer files and are used in the next step of the analysis process, scattering of the horn fields from the subreflector.

B. Subreflector Shape

First, however, the exact shape of the subreflector surface must be mathematically described. Figure 3 shows the schematic view of the subreflector with its hyperboloid section, two-segment vertex plate, and peripheral flange. The use of the computer program describing the subreflector shape is given in Ref. 6. The output of this program (the subreflector shape) is also used as an input to the subreflector scattering program.

A series of calculations was made at 8.4 GHz to examine the effect of a changing flange angle (Fig. 3, angle BE3) on noise temperature contribution from rear spillover and ground emission. The full use of this program is described later. The results are shown in Table 6. It is seen that unless the outer portion of the subreflector is "turned in" toward the main reflector, an unacceptably large amount of rear spillover results and substantially increases the system noise temperature. The existing design angle is 63.226°. The calculations

leading to the Table 6 values were made using subreflectors with no vertex plates. The effect on rear spillover (of neglecting the vertex plates) is negligible.

C. Scattering Program

The scattering program calculates the scattered field resulting from the corrugated horn (Section III.A) illuminating the subreflector (Section III.B). The scattered field contains components of the horn pattern also, so that the sidelobes of the horn pattern should not be disregarded even though they do not strike the subreflector. These sidelobes may be sensitive to a source of RFI within 20 degrees of the main antenna beam. This problem will be discussed later. In other words, the field sensitive to noise from the sky and ground exists in all space, in both the forward and rearward directions. A description of the scattering program is given in Ref. 7. This program is known in the Telecommunications Division as the Rusch Scattering Program, after W. V. T. Rusch, the originator.

Table 7 gives some of the pertinent input values used in the Rusch Scattering Program. A large number of the other input values are "administrative" and refer to the calculation technique rather than the geometry of the problem. Data file inputs to this program are the subreflector shape and the corrugated horn pattern. It is important to remember that input horn patterns at frequencies other than 2.3 or 8.4 GHz are from *misfocused* horns.

Figures 5 and 6 show the S-band and X-band amplitude patterns of the hyperboloid-scattered fields. A polar angle equal to 0° is toward the vertex of the main reflector as seen from the hyperboloid. A polar angle of 180° corresponds to the direction behind the subreflector; and the region 140° to 180° contains the sidelobes and diffracted pattern of the feedhorn.

It can be seen from Figs. 5 and 6 that RFI sources (e.g., radio stars) located approximately 20 degrees (polar angle 160 degrees) and 100 degrees (polar angle 80 degrees) from the main antenna beam (polar angle 180 degrees) may cause system noise temperature increases. The 20° peak of the scattered pattern is "forward spillover" and is caused primarily by power from the feedhorn passing beyond the edge of the subreflector. The 100° peak is "rear spillover" and comes about from scattered energy passing beyond the edge of the main reflector. The location of known radio noise sources must be monitored during SETI search procedures to avoid confusion and misinterpretation. Table 8 gives the amplitude and location (±0.5°) of the strong scattered sidelobe at 160 degrees polar angle (cf. Figs. 5 and 6).

The dip near the center of each pattern shows the effect of the vertex plate removing and redirecting energy which would otherwise strike the central cone and feed system. The steep taper in the 70°-80° range shows the effect of both the normal Cassegrain optics and the additional flange around the edge of the subreflector. The polar angle to the edge of the main reflector is 75.525°; the edge illumination power level is down approximately 15 dB at this angle.

The output of the scattering program is the far-field amplitude and phase of the field scattered from the subreflector. This field exists in all space (polar angle 0° to 180°); and a portion of it (that with the greatest amplitude) is intercepted by the main reflector. Also calculated by the program are numerous efficiencies pertaining to forward and rear spillover, non-uniform amplitude and phase illumination, and cross polarization. Quadripod blockage is neglected, as it is considered common to all frequencies and elevation angles. For each frequency, an overall aperture efficiency is calculated. This efficiency is not a function of elevation angle, and represents "how well" the illuminated main reflector utilizes the incident energy compared to a uniformly illuminated circular aperture of the same diameter.

The aperture efficiency is directly related to gain and is used as one of the gain components in the G/T figure-of-merit. The calculations yield typical aperture efficiencies in the range 70 to 80 percent for the frequencies studied. The aperture efficiencies (which are a function of frequency only) appear as the term "$\eta_{aperture}$" in Eq. (1).

D. Surface Efficiency

The effects of main reflector roughness and deviation from paraboloidal shape are accounted for by an "equivalent" Ruze formula (Ref. 8):

$$\frac{G}{G_0} = \exp\left[-\left(\frac{4\pi\epsilon}{\lambda}\right)^2\right] \qquad (2)$$

where

G/G_0 = fractional gain reduction

ϵ = rms surface roughness

λ = wavelength

A surface tolerance ϵ is chosen *a priori* to give the measured or expected gain reduction seen on the DSS-12 34-meter-type antenna. This equivalent surface tolerance is given in Table 9. The antenna surface is adjusted to have best shape at 30° elevation. Due to the behind-dish support structure, the worst shape occurs at 90° elevation. Typical fractional gains range

from 99% at low frequencies down to 80% at high frequencies and worst attitude shape. A nominal X-band fractional gain given in Ref. 4 for the specific case of a 34-meter reflex-feed antenna (e.g., DSS-12) is 0.88 for a 1-mm rms surface distortion due to wind, thermal, and gravity effects. The surface efficiency values determined as a function of frequency and elevation angle are directly related to the antenna gain and appear as the term "$\eta_{surface}$" in Eq. (1).

E. Ground and Atmosphere Noise Temperature

Figure 7 shows typical antenna rays which contribute to noise from the ground and atmosphere. Ray 1 is scattered from the subreflector edge and sees the hot ground. Ray 2 is part of the horn pattern and sees the atmosphere. Ray 3 (part of the main antenna beam) strikes the surface of the main reflector and is reflected upward at the elevation angle of the antenna. Ray 4 is scattered from the subreflector edge and sees the sky. The net noise temperature from the effect of all these rays can be calculated from the expression

$$T_{noise} = \frac{\iint T_{source}(\theta,\phi)\, G(\theta,\phi)\, dA}{\iint G(\theta,\phi)\, dA} \qquad (3)$$

where

T_{source} = ground or atmosphere equivalent blackbody noise temperature

G = scattered field strength (gain) in direction of source

dA = unit area in direction of source

The geometry is complex, but the results obtained as a function of elevation angle (at 2.3 or 8.4 GHz) agree quite well with experiment and simpler estimates.

The ground is considered to have an average equivalent blackbody noise temperature of 240 K. The equivalent blackbody noise temperature of the ground is a function of its emissivity, which in turn is a complex function of the dielectric constant of the ground, grazing angle of the impinging ray, polarization, and frequency. For rough surfaces, frequencies greater than 1 GHz, and grazing angles greater than 10°, reflection coefficients of 0.0 to 0.4 are found. This would yield blackbody temperatures of 300 K down to 180 K, respectively. Ground emissivity is discussed in much detail in Ref. 9.

The atmosphere is modeled to have a zenith noise temperature contribution (for an antenna at approximately 1 km above sea level) at S-band of 2.0 to 2.1 K and at X-band of 2.5 to 2.75 K from lowest to highest frequencies. The clear-sky atmospheric noise contribution arises from oxygen (predominantly, below 10 GHz) and water vapor. The elevation angle dependence of atmospheric noise temperature is modeled as the inverse sine of the elevation angle, up to a maximum of 19.1 airmasses (equivalent to an elevation angle of 3°), to account for the round earth.

F. Quadripod Scatter Noise Temperature

Some amount of power received by the feedhorn arrives from the ground via scattering from the quadripod structure. This ground contribution is considered separately from the spillover ground noise described previously. Estimates of the noise temperature contribution from this source have been made by Potter (Ref. 10) for a 64-meter antenna. By a careful process of measurement and subtraction of known effects, the elevation angle effects were determined. It is felt that these values will apply to the 34-meter antenna system also. This component of noise temperature has not been measured separately; however, overall system noise temperature measurements at various elevation angles confirm the results obtained in Ref. 10. It should be mentioned again that quadripod noise temperature is assumed to be a function of elevation angle only, not frequency, to within experimental error. The noise contribution ranges from 2.5 K at zenith to 6 K at 10° elevation.

G. Baseline Noise Temperature

Part of the figure-of-merit calculation (Eq. [1]) is the determination of the non-changing portion of the system noise temperature, due to preamplifier, waveguide, and cosmic noise contributions. Since the baseline *system* noise temperatures are known, it is a simple matter to subtract out the ground, atmosphere, and quadripod contributions calculated here in order to arrive at the non-changing component. The baseline values used here are 14.81 K (S-band) and 18.25 K (X-band).

Tables 10 through 14 show sample calculated results of the G/T components described above. Complete listings for all frequencies and elevation angles are too lengthy to present here. These tables show the general variations of the components over extreme ranges of frequency and elevation angle.

IV. Results

As discussed in Section III, a G/T figure-of-merit was calculated for each frequency and elevation angle considered. This figure-of-merit was normalized to the value obtained at zenith and 2.3 (S-band) or 8.4 (X-band) GHz. Table 15 contains the complete relative G/T figures-of-merit (in dB) as a function of frequency and elevation angle. It can be seen that for the X-band case at the higher elevation angles (50°-80°), G/T performance is increased over that at zenith. This is due primarily to the decreased ground contribution and increased surface

efficiency. The maximum G/T increase is found to be about 0.3 dB. For S-band above 30° elevation, and X-band above 20° elevation, G/T degradation is found to be less than about 1 dB. Figures 8 through 12 show the aperture and surface efficiency, ground and atmospheric noise, and quadripod scatter noise, respectively, for the nominal 2.3 and 8.4 GHz frequencies. Figure 13 shows the G/T figures-of-merit at S-band for various elevation angles. Figure 14 shows the same for X-band.

From Figs. 13 and 14, it can be seen that given elevation angle limits and signal-to-noise ratio margins above some desired threshold, an estimate can be made of the number of feedhorns needed to cover the 1 to 10 GHz frequency range. Fortunately, feed system performance is not a strong function of frequency over the operating range of a single horn. The primary causes of G/T degradation are the three elevation-dependent noise temperature contributions from the ground, atmosphere, and quadripod scatter.

It may be concluded that the DSN 34-meter HA-DEC subnet (or 26-meter antennas) could, at least down to the feedhorn output, provide significant bandwidth and high G/T performance, even using the somewhat restrictive DSN standard corrugated horn design. Techniques to achieve wider bandwidth horns are now available, but not yet proven on a DSN antenna. The reader should note, however, that the design of wideband (1.4:1 or greater bandwidth) low-noise preamplifier, polarizer, and orthomode components is not well understood. The above analysis defers performance study of these important components. Further studies will provide a "balanced" design capable of 1 to 10 GHz bandwidth coverage in a cost effective way. Meanwhile, certain planning functions for SETI can proceed, based on the analysis presented here.

Acknowledgment

The author wishes to thank Eduardo Andres who carried out the numerous computer calculations and generated all the plots. Carole Devereux typed this report and graciously tolerated my numerous revisions. Dan Bathker and Bill Williams generously provided much needed technical support and guidance.

References

1. F. Drake, J. H. Wolfe, and C. L. Seeger, SETI Science Working Group Report, NASA Tech. Paper 2244, 1984.

2. S. Gulkis, Note on the Optimum Search Strategy for Uniformly Distributed CW Transmitters, *TDA Progress Report 42-77*, Jet Propulsion Laboratory, Pasadena, Calif., 1984, pp. 144-150.

3. N. A. Renzetti, C. T. Stelzried, et al., The Deep Space Network – A Radio Communications Instrument for Deep Space Exploration, *JPL Publication No. 82-104*, Jet Propulsion Laboratory, Pasadena, Calif., July 15, 1983.

4. D. L. Nixon and D. A. Bathker, S-/X-Band Microwave Optics Design and Analysis for DSN 34-Meter-Diameter Antenna, *DSN Progress Report 42-41*, Sept. 15, 1977, Jet Propulsion Laboratory, Pasadena, Calif., pp. 146-165.

5. Jet Propulsion Laboratory, DSN/Flight Project Interface Design Document 810-5, Rev. D., TCIs-10, -20, -30 (internal document), November 1984, Pasadena, Calif.

6. A. Ludwig, editor, Computer Programs for Antenna Feed System Design and Analysis, Vol. I, *JPL Technical Report No. 32-979*, April 15, 1967, Jet Propulsion Laboratory, Pasadena, Calif., pp. 27-29.

7. A. Ludwig and W. V. T. Rusch, Digital Computer Analysis of a Subreflector of Complex Shape, *JPL Technical Report No. 32-1190*, November 15, 1967, Jet Propulsion Laboratory, Pasadena, Calif.

8. J. Ruze, Antenna Tolerance Theory – A Review, *Proc. IEEE*, Vol. 54, No. 4, April 1966, pp. 633-640.

9. H. Reed and C. Russell, *Ultra High Frequency Propagation*, Wiley and Sons, New York, 1953.

10. P. D. Potter, Efficient Antenna Systems: Calibration of the Mars Deep Space Station 64-m Antenna System Noise Temperature Degradation Due to Quadripod Scatter, *JPL Technical Report 32-1526*, Vol. XVI, August 15, 1973, Jet Propulsion Laboratory, Pasadena, Calif., pp. 22-29.

Table 1. Dimensions for 34-meter symmetric antenna configuration (cf. Fig. 2)

Parameter	Dimension
Diameter	149.532 in.
A	101.6233 in.
C	138.000 in.
V	158.468 in.
TH1	75.5 deg
TH2	75.525 deg
AL2	13.500 deg
AL3	15.675 deg
BE3	63.226 deg

Table 2. Dimensions for 34-meter symmetric subreflector with vertex plate and peripheral flange (cf. Fig. 3)

Parameter	Dimension
C	138.000 in.
A	101.6233 in.
D	0.873 in.
AL1	0.92065 deg
AL2	13.500 deg
AL3	15.675 deg
BE1	81.903 deg
BE2	81.175 deg
BE3	63.226 deg

Table 3. Components of gain and noise temperature calculated for G/T figure-of-merit determination

Components	Function of: Frequency	Function of: Elevation Angle
Gain		
Aperture efficiency	Yes	No
Surface efficiency	Yes	Yes
Noise Temperature		
Ground noise	Yes	Yes
Atmospheric noise	Yes	Yes
Quadripod scatter noise	No	Yes
Maser, waveguide, cosmic background (T_{base})	Constant for each band	

Table 4. S- and X-band corrugated horn design values

Parameter	S-Band	X-Band
Phasing section length	0.0 in.	0.0 in.
Diameter of phasing section and small end of flare	5.039 in.	1.369 in.
Flare length	95.928 in.	26.06 in.
Aperture diameter	26.051 in.	7.077 in.
Groove depth in phasing section and flare	1.583 in.	0.430 in.
Frequency[a]	1.8–2.7 GHz[b]	7.0–9.4 GHz
Phase center position inside horn aperture at nominal design frequency	8.3874 in. at 2.3 GHz	2.2129 in. at 8.4 GHz

[a]The frequency is chosen to reflect the inherent bandwidth limitations of the DSN corrugated horns.
[b]The modeled range would be 1.9–2.6 GHz

Table 5. Characteristics of corrugated horn illumination patterns

Frequency, GHz	E-Plane 3 dB Beamwidth Half-Angle, deg	E-Plane Taper at 16° (Subreflector Edge), dB	Phase Center Position Inside Aperture, in.
1.8	9.6	-8.8	3.605
1.9	9.1	-10.1	4.305
2.0	8.5	-11.5	5.113
2.1	8.1	-13.0	6.046
2.2	7.7	-14.6	7.128
2.3 (Design freq.)	7.3	-16.3	8.387
2.4	7.0	-18.0	9.852
2.5	6.7	-19.6	11.556
2.6	6.4	-20.8	13.506
2.7	6.2	-21.6	15.721
7.0	9.0	-10.1	1.173
7.2	8.8	-10.9	1.288
7.4	8.5	-11.7	1.414
7.6	8.3	-12.5	1.548
7.8	8.0	-13.3	1.695
8.0	7.8	-14.2	1.854
8.2	7.6	-15.1	2.026
8.4 (Design freq.)	7.4	-16.0	2.213
8.6	7.2	-17.0	2.416
8.8	7.1	-17.9	2.636
9.0	6.9	-18.8	2.875
9.2	6.7	-19.6	3.131
9.4	6.6	-20.3	3.404

Table 6. Ground noise temperature contribution for zenith-pointing antenna, as a function of subreflector flange angle

Flange Angle, deg	Ground Noise Temperature, K
71.5	1.413
65.0	1.126
63.226 (34-m design value)	1.339
58.984 (tangent to hyperboloid)	8.348

Table 7. Input values for Rusch Subreflector Scattering Program

Parameter	Meaning, value
DIST	Subreflector focal length (2C), 276.0 in.
BLK	Half blockage angle of subreflector shadow at vertex of main reflector, 9.780°
X1	Lower limit of integration (subreflector edge), 164.21°
X2	Intermediate limit of integration, 172.0°
X3	Upper limit of integration, 180.0°

Table 8. Sidelobe characteristics near the main beam of the 34-meter antenna

Frequency, GHz	Sidelobe Position Relative to Main Beam, deg (±0.5°)	Amplitude of Sidelobe Peak, dBi
1.8	20	6.0
1.9	19	4.9
2.0	20	4.0
2.1	19	3.3
2.2	19	2.7
2.3	18	2.6
2.4	19	2.5
2.5	18	2.6
2.6	19	2.1
2.7	17	2.4
7.0	19	7.5
7.2	19	7.0
7.4	19	6.3
7.6	18	5.7
7.8	18	5.1
8.0	18	4.2
8.2	18	3.4
8.4	18	3.1
8.6	18	3.0
8.8	18	2.6
9.0	18	2.1
9.2	18	1.8
9.4	18	1.9

Table 9. Equivalent surface tolerance for 34-meter HA-DEC antenna, e.g., DSS-12

Elevation Angle, deg	RMS Surface Tolerance, in.
0	0.0375
10	0.0330
20	0.0300
30	0.0293 (3/4 mm)
40	0.0300
50	0.0315
60	0.0345
70	0.0375
80	0.0420
90	0.0465

Table 10. Aperture efficiency as a function of frequency and elevation angle

Frequency, GHz	Elevation Angle, deg			
	10	20	30	90
1.8	0.760	0.760	0.760	0.760
2.3	0.785	0.785	0.785	0.785
2.7	0.707	0.707	0.707	0.707
7.0	0.710	0.710	0.710	0.710
8.4	0.739	0.739	0.739	0.739
9.4	0.711	0.711	0.711	0.711

Table 11. Surface efficiency as a function of frequency and elevation angle

Frequency, GHz	Elevation Angle, deg			
	10	20	30	90
1.8	0.996	0.997	0.997	0.992
2.3	0.993	0.995	0.995	0.987
2.7	0.991	0.993	0.993	0.982
7.0	0.941	0.951	0.953	0.887
8.4	0.916	0.930	0.933	0.841
9.4	0.896	0.914	0.917	0.805

Table 12. Ground noise temperature (K) as a function of frequency and elevation angle

Frequency, GHz	Elevation Angle, deg			
	10	20	30	90
1.8	11.05	5.28	3.89	5.86
2.3	4.33	1.87	1.35	1.84
2.7	2.79	0.59	0.32	0.28
7.0	7.93	2.45	1.52	1.94
8.4	3.66	1.54	0.96	1.34
9.4	2.67	0.92	0.56	0.68

Table 13. Atmospheric noise temperature (K) as a function of frequency and elevation angle

Frequency, GHz	Elevation Angle, deg			
	10	20	30	90
1.8	12.77	7.05	4.79	2.91
2.3	12.32	6.47	4.39	2.35
2.7	12.40	6.37	4.29	2.14
7.0	15.50	8.27	5.49	2.91
8.4	15.73	8.22	5.57	2.92
9.4	16.18	8.38	5.67	2.89

Table 14. Quadripod scatter noise temperature (K) as a function of frequency and elevation angle

Frequency, GHz	Elevation Angle, deg			
	10	20	30	90
1.8	6.00	5.70	4.70	2.50
2.3	6.00	5.70	4.70	2.50
2.7	6.00	5.70	4.70	2.50
7.0	6.00	5.70	4.70	2.50
8.4	6.00	5.70	4.70	2.50
9.4	6.00	5.70	4.70	2.50

Table 15. G/T figures-of-merit (dB) relative to nominal values at zenith and 2.3 GHz (S-Band) or 8.4 GHz (X-Band)

Frequency, GHz	Elevation Angle, deg									
	0	10	20	30	40	50	60	70	80	90
1.8	-5.487	-3.272	-1.935	-1.272	-0.959	-0.784	-0.695	-0.707	-0.955	-0.956
1.9	-5.227	-2.935	-1.696	-1.071	-0.768	-0.596	-0.497	-0.494	-0.706	-0.696
2.0	-5.035	-2.684	-1.498	-0.894	-0.595	-0.413	-0.307	-0.288	-0.466	-0.439
2.1	-4.925	-2.509	-1.359	-0.764	-0.462	-0.282	-0.164	-0.130	-0.275	-0.244
2.2	-4.879	-2.420	-1.281	-0.696	-0.390	-0.205	-0.079	-0.036	-0.150	-0.113
2.3	-4.883	-2.385	-1.242	-0.663	-0.351	-0.163	-0.026	0.032	-0.043	0.000
2.4	-4.941	-2.405	-1.252	-0.679	-0.361	-0.163	-0.022	0.052	0.012	0.045
2.5	-5.033	-2.464	-1.301	-0.733	-0.415	-0.215	-0.062	0.017	-0.002	0.027
2.6	-5.155	-2.551	-1.381	-0.816	-0.494	-0.290	-0.130	-0.044	-0.042	-0.012
2.7	-5.316	-2.678	-1.495	-0.930	-0.605	-0.397	-0.237	-0.145	-0.126	-0.106
7.0	-4.936	-2.490	-1.060	-0.417	-0.102	0.068	0.163	0.176	0.036	-0.045
7.2	-4.834	-2.335	-0.969	-0.341	-0.045	0.125	0.211	0.229	0.084	-0.001
7.4	-4.776	-2.231	-0.914	-0.302	-0.005	0.159	0.244	0.249	0.104	0.017
7.6	-4.737	-2.158	-0.885	-0.275	0.027	0.190	0.273	0.283	0.143	0.046
7.8	-4.711	-2.099	-0.859	-0.256	0.039	0.201	0.282	0.284	0.134	0.036
8.0	-4.696	-2.048	-0.834	-0.236	0.062	0.218	0.300	0.302	0.155	0.052
8.2	-4.718	-2.039	-0.842	-0.240	0.054	0.212	0.290	0.287	0.140	0.033
8.4	-4.747	-2.047	-0.860	-0.263	0.031	0.192	0.265	0.261	0.113	0.000
8.6	-4.792	-2.065	-0.876	-0.286	0.011	0.171	0.244	0.243	0.095	0.012
8.8	-4.855	-2.104	-0.910	-0.325	-0.029	0.130	0.202	0.199	0.052	-0.066
9.0	-4.905	-2.125	-0.935	-0.354	-0.053	0.106	0.172	0.171	0.025	-0.096
9.2	-4.972	-2.168	-0.974	-0.390	-0.093	0.067	0.136	0.131	-0.017	-0.151
9.4	-5.082	-2.258	-1.045	-0.464	-0.163	-0.008	0.056	0.050	-0.094	-0.238

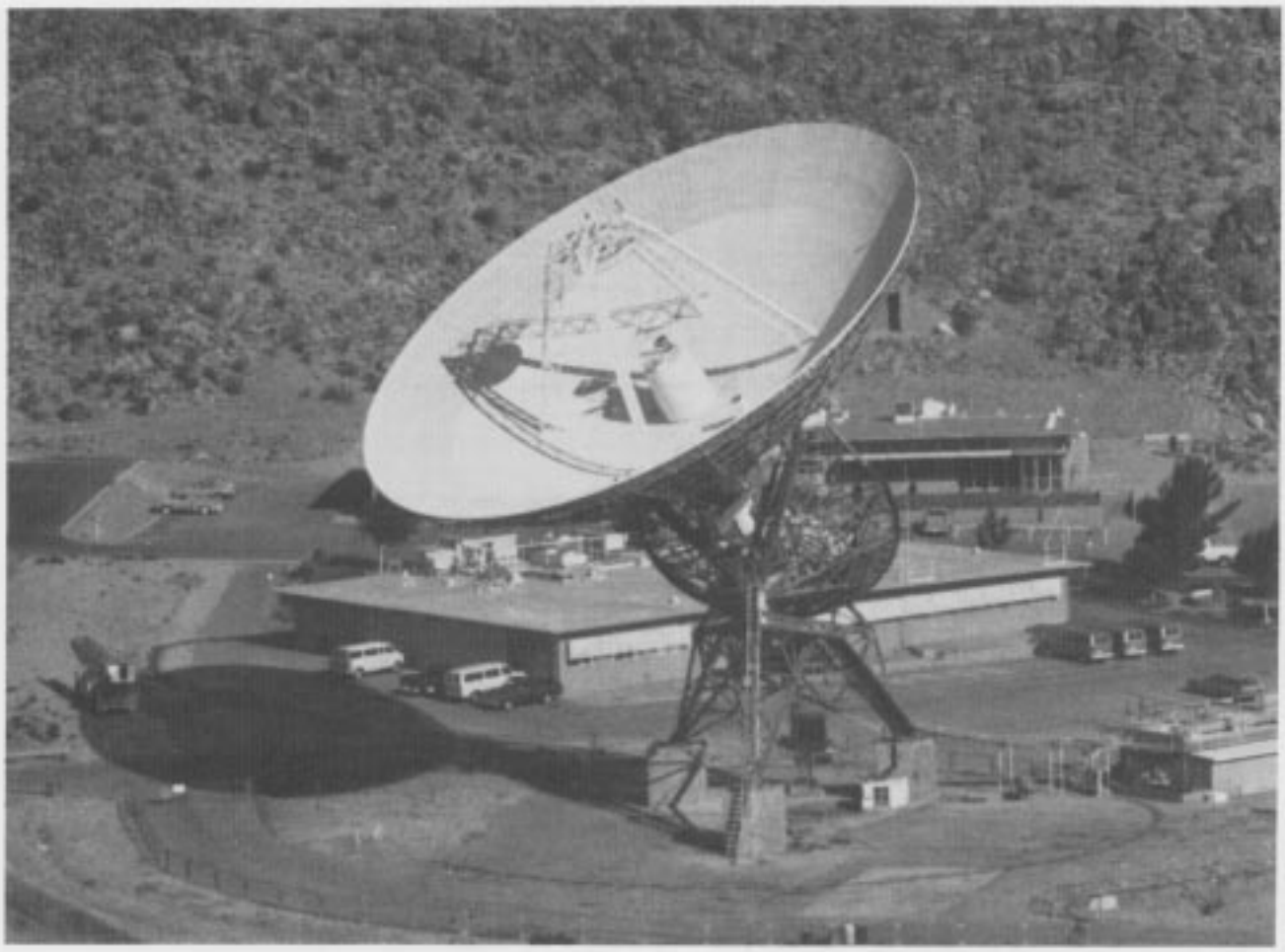

Fig. 1. DSS-12 34-meter antenna at Goldstone, in S/X reflex feed configuration

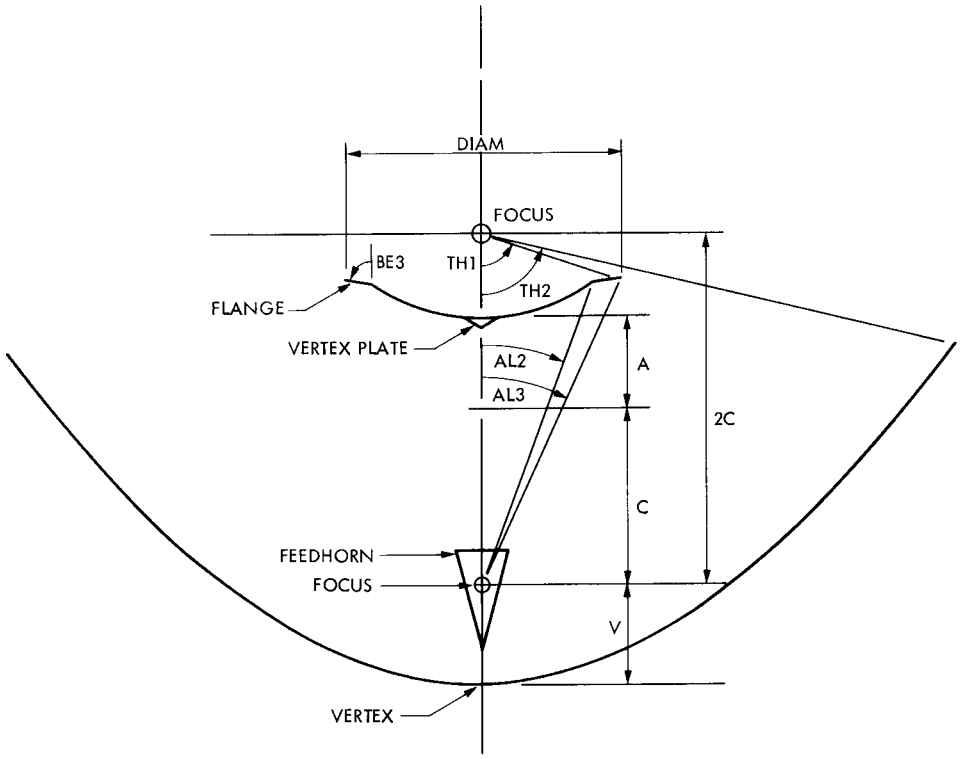

Fig. 2. Diagram of typical symmetric antenna configuration (cf. Table 1 for 34-meter antenna dimensions)

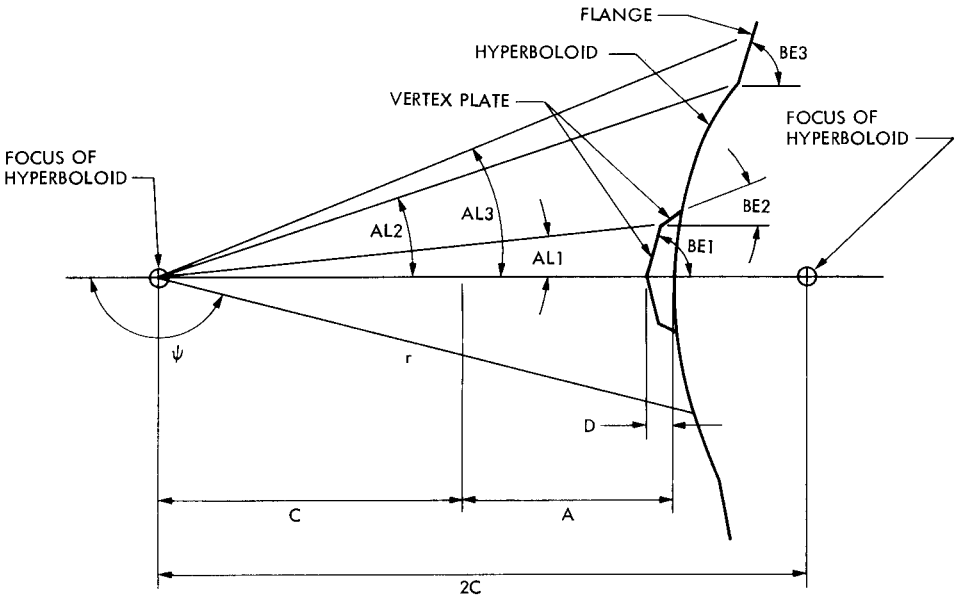

Fig. 3. Diagram of typical symmetric subreflector configuration (cf. Table 2 for 34-meter subreflector dimensions)

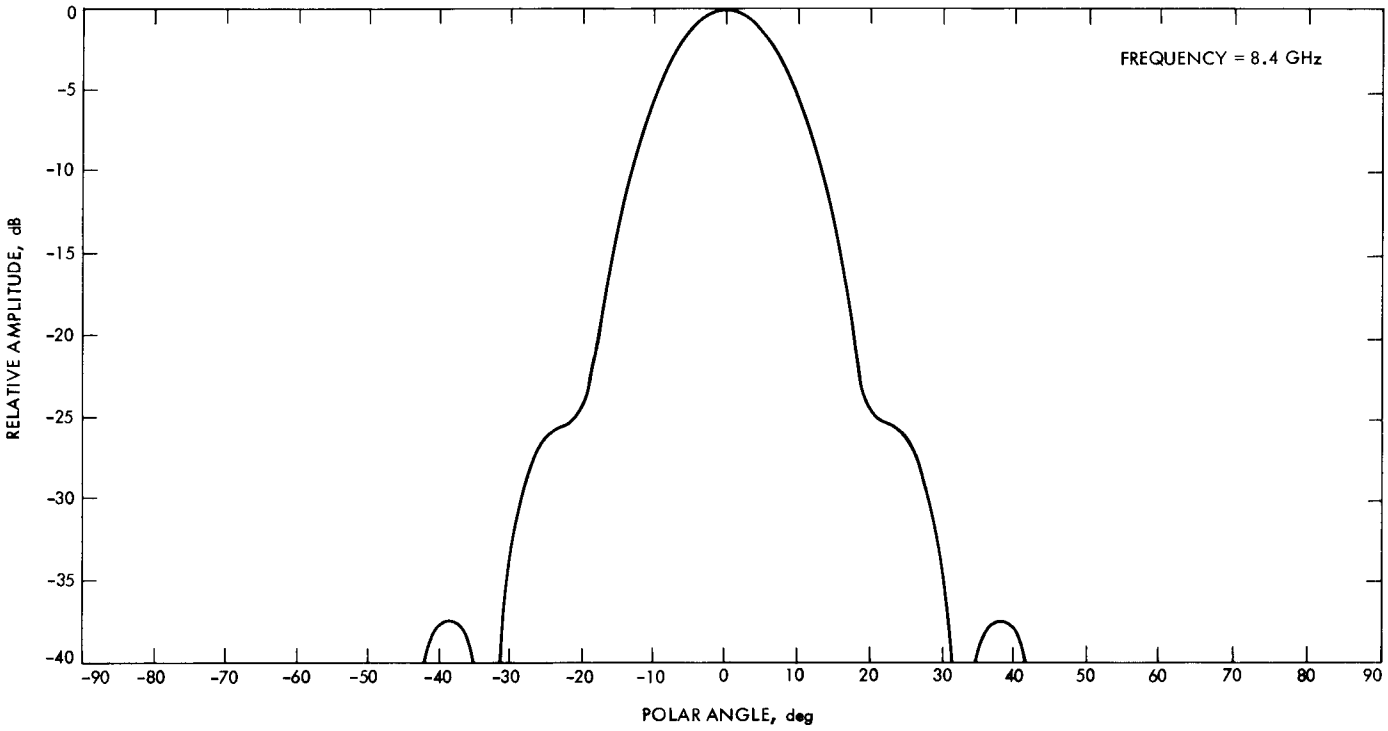

Fig. 4. Typical corrugated feedhorn amplitude pattern, S- and X-band (8.4 GHz shown)

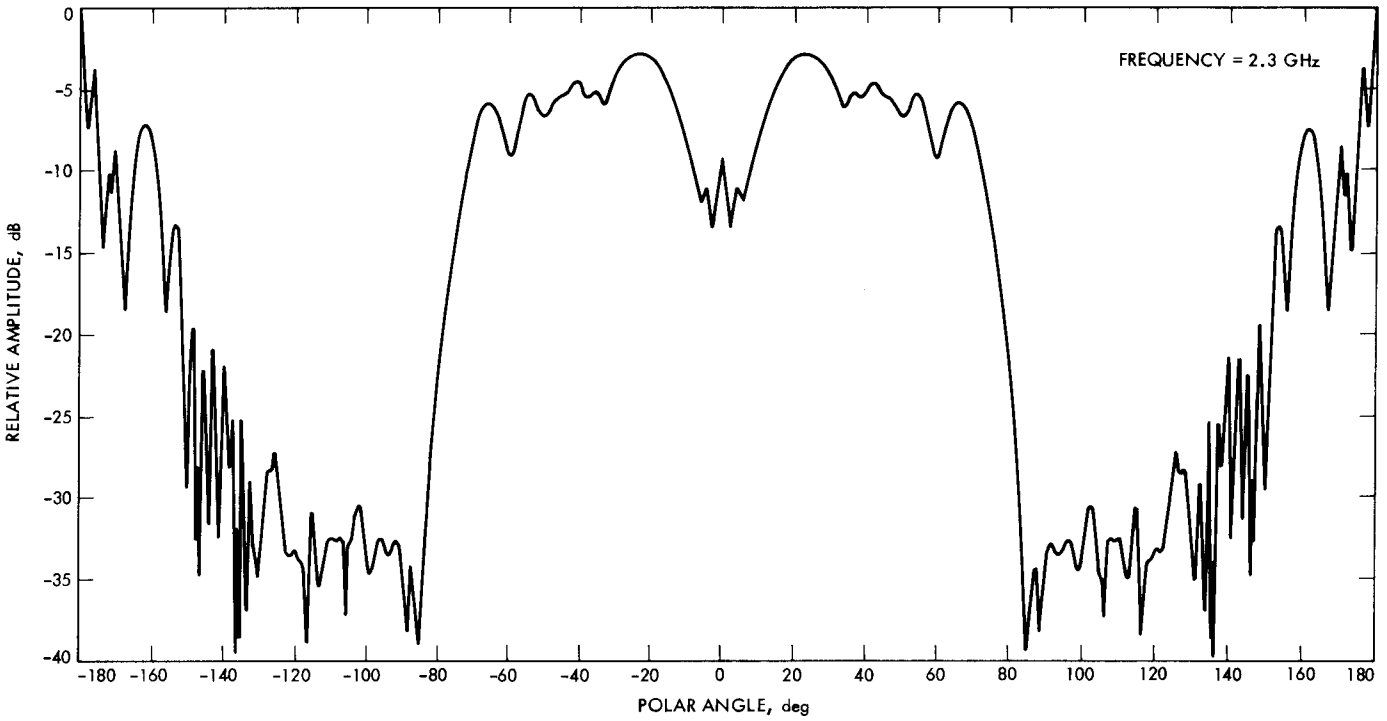

Fig. 5. Typical S-band scattered field from symmetric subreflector in 34-meter antenna configuration

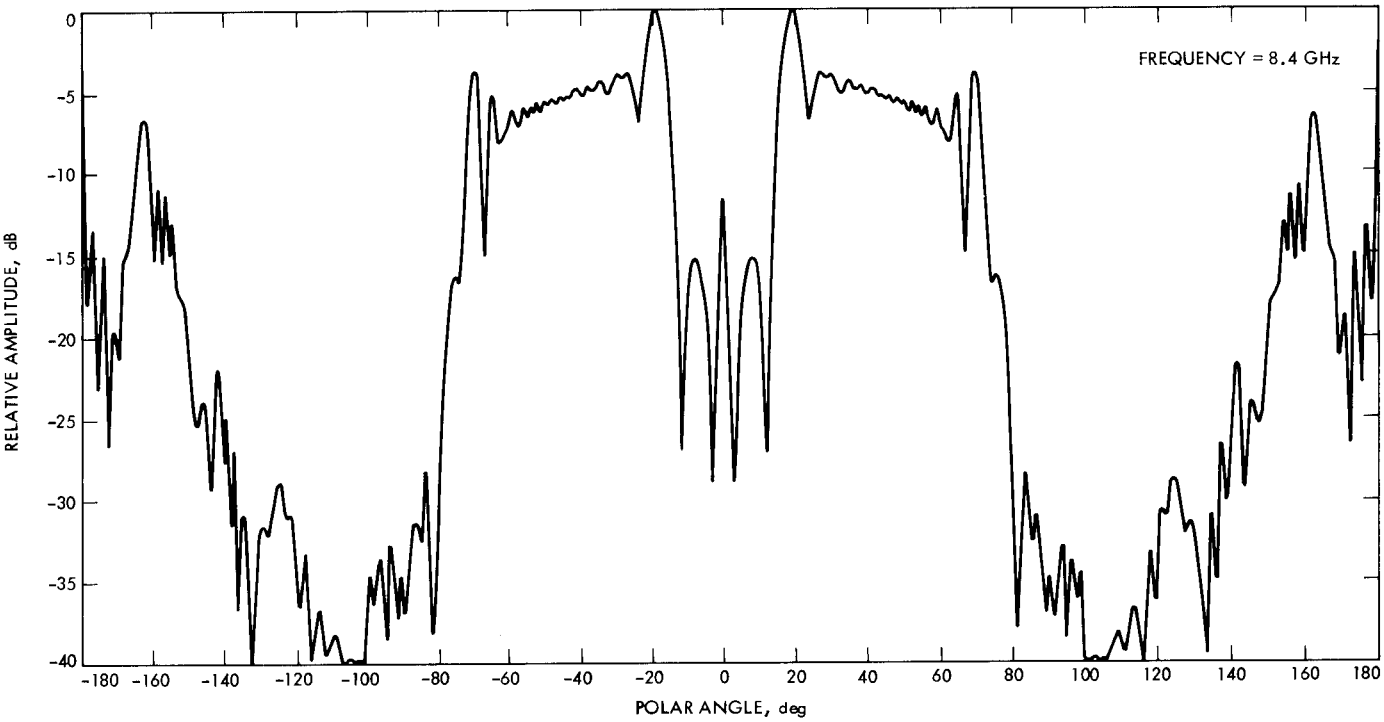

Fig. 6. Typical X-band scattered field from symmetric subreflector in 34-meter antenna configuration

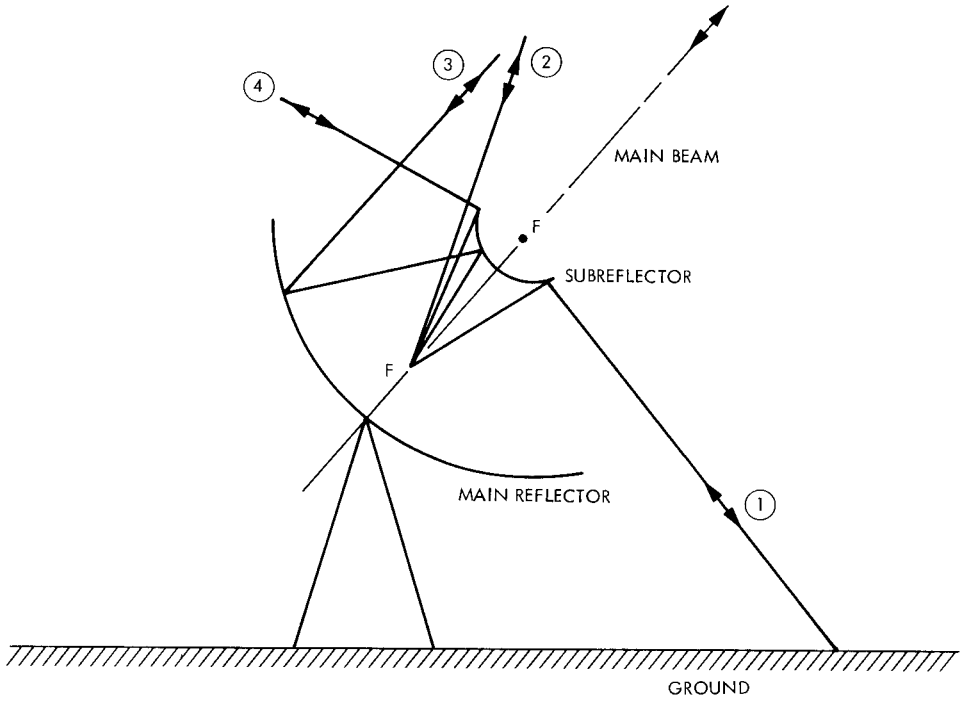

Fig. 7. Schematic view of ground and atmosphere contribution to system noise temperature

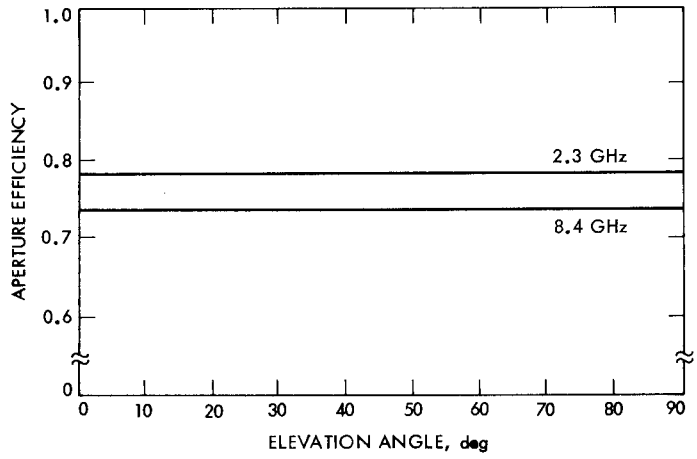

Fig. 8. Aperture efficiency at 2.3 and 8.4 GHz as a function of elevation angle

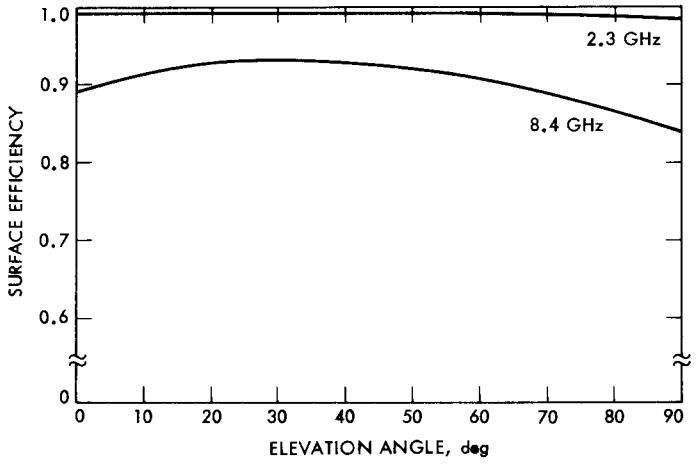

Fig. 9. Surface efficiency at 2.3 and 8.4 GHz as a function of elevation angle

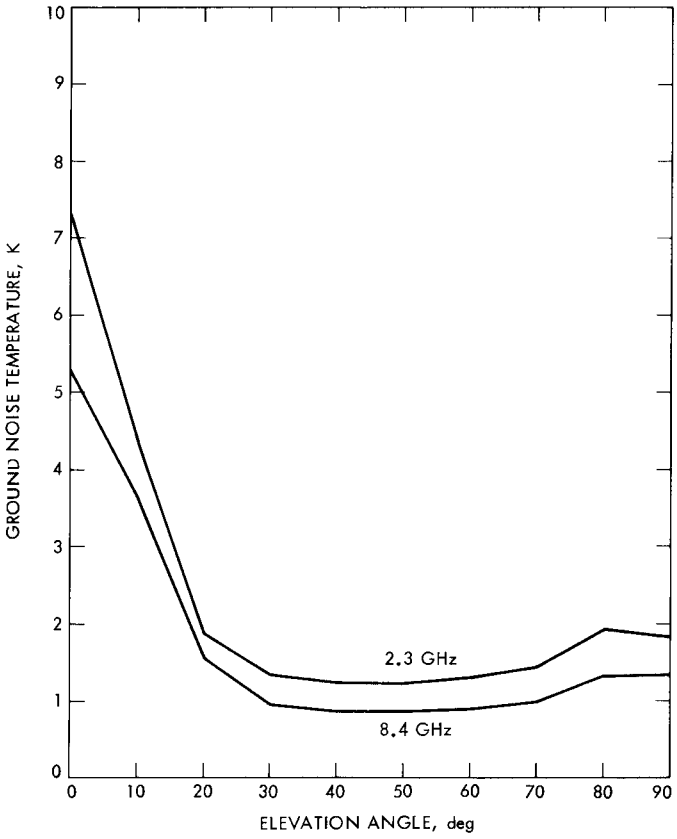

Fig. 10. Ground noise temperature at 2.3 and 8.4 GHz as a function of elevation angle

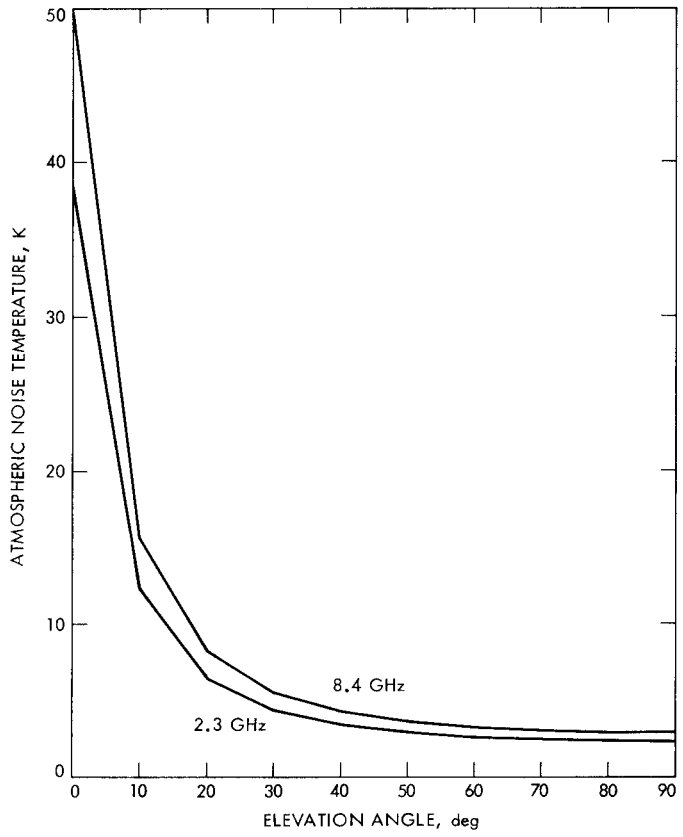

Fig. 11. Atmospheric noise temperature at 2.3 and 8.4 GHz as a function of elevation angle

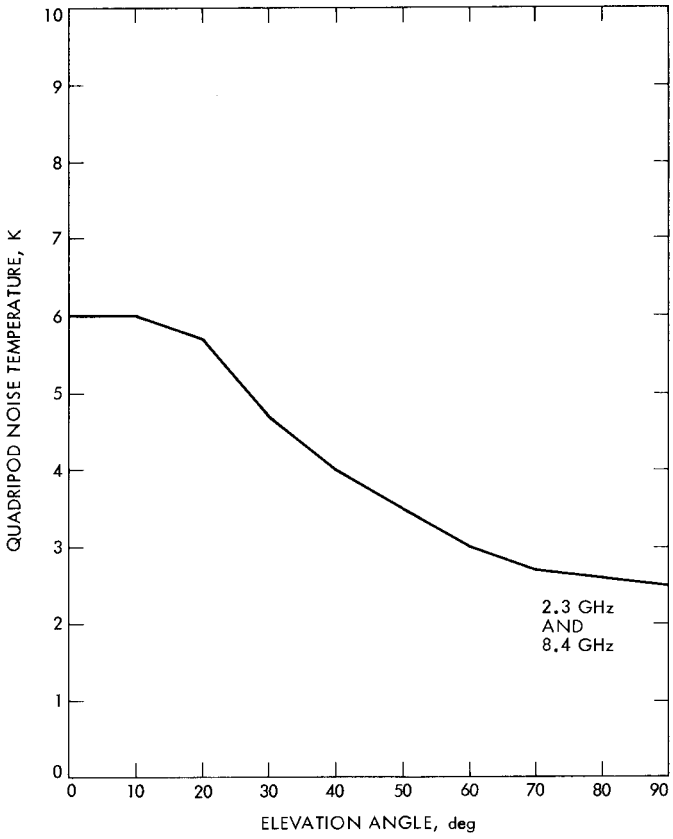

Fig. 12. Quadripod scatter noise temperature at 2.3 and 8.4 GHz as a function of elevation angle

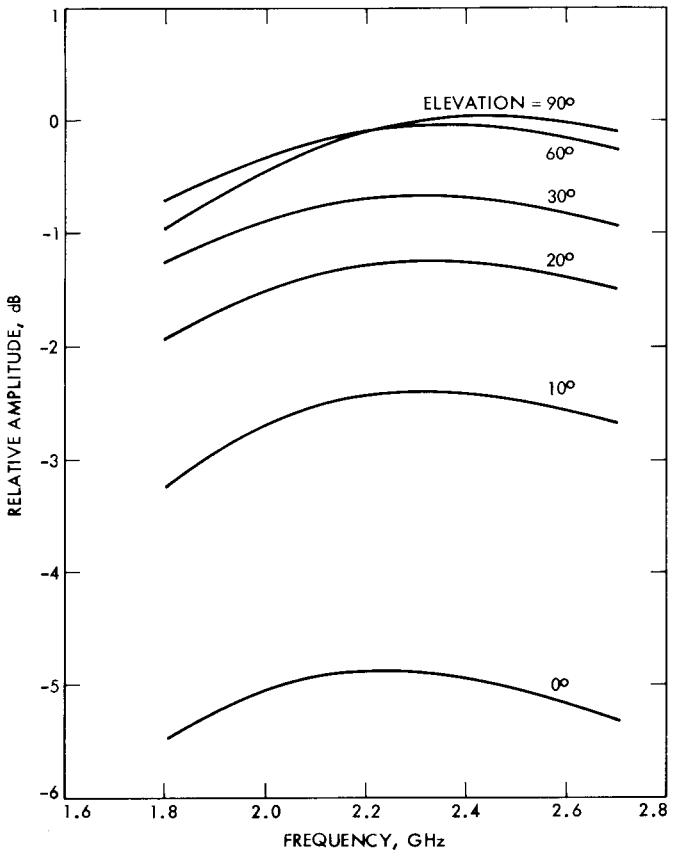

Fig. 13. G/T figure-of-merit for S-band relative to that at zenith and 2.3 GHz (cf. Table 15)

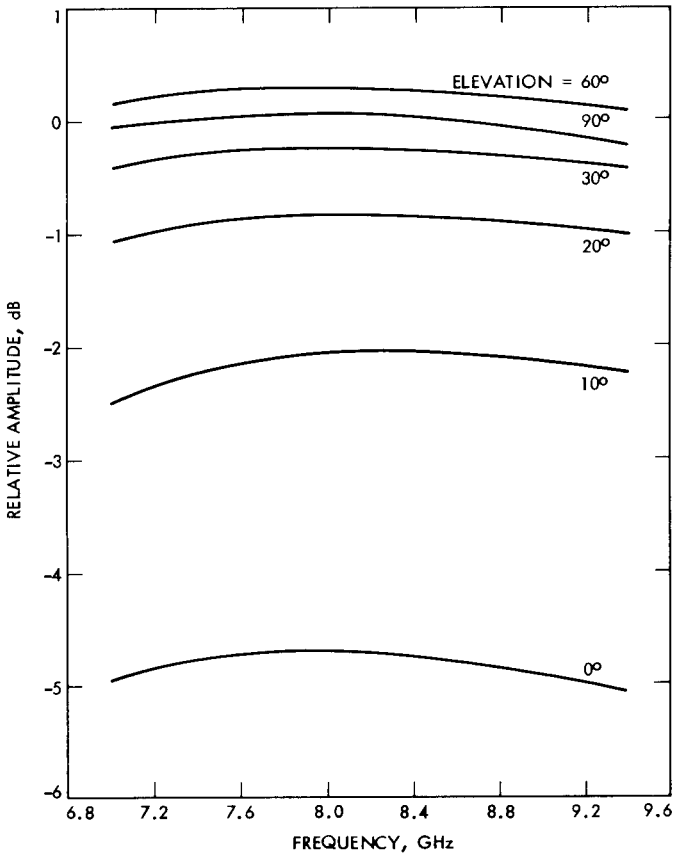

Fig. 14. G/T figure-of-merit for X-band relative to that at zenith and 8.4 GHz (cf. Table 15)